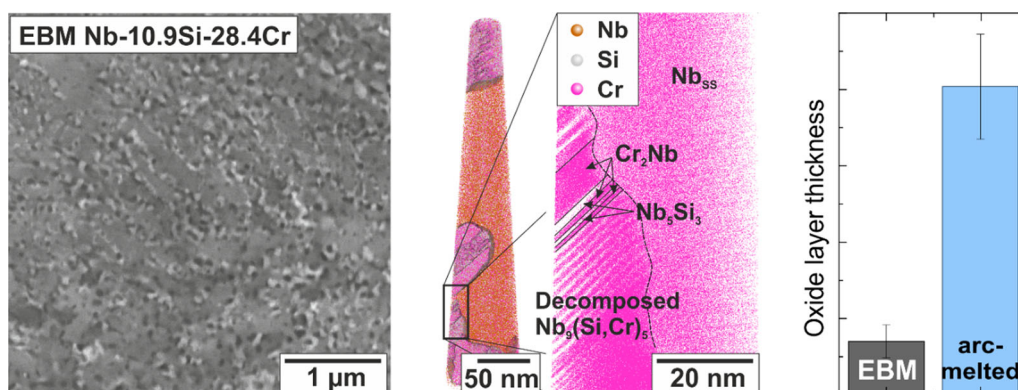


Nanostructuring of Nb-Si-Cr Alloys by Electron Beam Melting to Improve the Mechanical Properties and the Oxidation Behavior



A. FÖRNER, J. VOLLHÜTER, D. HAUSMANN, C. ARNOLD, P. FELFER, S. NEUMEIER, and M. GÖKEN

Materials processed by additive manufacturing often exhibit a very fine-scaled microstructures due to high cooling rates in the process. In this study, single-layer surface electron beam melting is used to create very high cooling rates similar to additive manufacturing processes to investigate the resulting microstructure. In the case of Nb-Si-Cr *in-situ* composites, a nano-scaled eutectic microstructure is beneficial for improving the mechanical and oxidation properties. Fast solidification results in the formation of supersaturated phases of Nb_{ss} and Cr₂Nb with phase diameters down to 10 nm as well as in the stabilization of the metastable Nb₉(Cr,Si)₅ phase at room temperature. After processing with different solidification rates, the decomposition of the Nb₉(Cr,Si)₅ phase has been studied in detail with atom probe microscopy. The stabilization of mixed silicide phases by electron beam melting shows a new pathway for improving hardness and enhancing oxidation resistance of nanostructured eutectic *in-situ* composites, by which the inherent weaknesses of Nb-Si-Cr can be overcome without further alloying elements.



<https://doi.org/10.1007/s11661-021-06516-x>
© The Author(s) 2021

I. INTRODUCTION

IN order to build more efficient engines and gas turbines, high-temperature structural materials with increased maximum service temperature are required. Conventional nickel-based superalloys cannot be used above 85 pct of the melting point due to severe softening.^[1] As an alternative, alloys in the niobium-silicon (Nb-Si) system with a much higher melting point were already considered 30 years ago. Among them are *in-situ* composites which are composed of a Niobium (Nb) solid solution phase (Nb_{ss}), strengthened by the

A. FÖRNER, J. VOLLHÜTER, D. HAUSMANN, P. FELFER, S. NEUMEIER, and M. GÖKEN are with the Department of Materials Science & Engineering, Institute I: General Materials Properties, Friedrich-Alexander-Universität Erlangen-Nürnberg, Martensstraße 5, 91058 Erlangen, Germany. Contact e-mail: andreas.foerner@fau.de. C. ARNOLD is with the Department of Materials Science & Engineering, Chair for Materials Science and Engineering for Metals (WTM), Friedrich-Alexander-Universität Erlangen-Nürnberg, Martensstraße 5, 91058 Erlangen, Germany.

Manuscript submitted May 27, 2021; accepted October 25, 2021.

Article published online November 13, 2021

intermetallic Nb₅Si₃ phase. The microstructure is formed by solidification of a hypoeutectic alloy with a eutectic phase transition (L → (Nb) + Nb₃Si) at 1920 °C followed by a eutectoid reaction (Nb₃Si → (Nb) + Nb₅Si₃) at 1770 °C.^[2,3] The high melting point above 2400 °C and their light weight with a density of approximately 7 g/cm³ are beneficial for the application at high temperatures.^[1,4-6] Unfortunately, the low fracture toughness of Nb₅Si₃ of around 3 MPam^{1/2} at room temperature and poor oxidation resistance of the Nb-rich solid solution limit their application.^[7-9] Many researchers have investigated the influence of different alloying elements like Ti, Cr, Al, Hf, Mo, W, and V in ternary, quaternary, or even more complex alloys to improve these properties.^[1,2,4,8,10-16] The addition of Cr to the Nb-Si system is a promising approach, leading to a ternary eutectic at Nb-10.9Si-28.4Cr (composition given in at. pct).^[4] This ternary eutectic is located in the Nb-rich corner of the phase diagram, where the stable phases at room temperature are Nb_{ss}, Nb₅Si₃, and Cr₂Nb.^[10,17,18] The metastable silicide phase Nb₉(Cr,Si)₅ can occur, but decomposes to Nb_{ss}, Nb₅Si₃, and Cr₂Nb at a heat treatment at 1300 °C.^[4] A eutectic microstructure with a silicide matrix phase strengthened by the Cr₂Nb Laves phase is formed which is ductilized by the Nb solid solution phase. Due to the silicide phases, the eutectic alloy exhibits an enhanced oxidation resistance, creep strength, and fracture toughness compared to single-phase Nb alloys.^[1,7,11,19-25] Depending on the Si and the Cr content in the alloy, different silicide phases have been reported. Nb₅Si₃ is found in most alloys, whereas Nb₉Cr₄Si, Nb₉Cr₂Si₃, and Nb₉(Cr,Si)₅ are only present in eutectic-near compositions. However, there is a controversial discussion about the existence of an equilibrium state of Nb₉Cr_xSi_y (where $x + y = 5$) phases that are stable at room temperature,^[4,13,15,26,27] especially due to the coexistence of this phase with an unknown mixed silicide phase with an Nb content of about 54 at. pct.^[4,10]

The mechanical properties like fracture toughness of *in-situ* composites strongly depend on the geometry and the volume fraction of ductile and brittle phases. A common approach for creating well-aligned microstructures is directional solidification, where oriented phases can be achieved to promote crack deflection and crack tip blunting.^[2,12,22,28] However, their challenging processability by casting leads to the consideration of methods with unlimited design freedom like laser or electron beam-based additive manufacturing.^[1,2] In such processes, also grain refinement due to high cooling rates can be achieved, which is beneficial for enhancing mechanical properties. Guo *et al.* showed remarkable improvement in oxidation resistance for a fine-structured Nb-18Si-24Ti-2Cr-2Al-2Hf alloy, processed by selective laser beam melting (SLM) due to small Nb_{ss} phases, high amounts of interfaces, great surface area of the silicon phases, and thus a low oxygen partial pressure at the metal-oxide interface.^[29]

This study aims towards the creation of a nanostructured and aligned eutectic Nb-10.9Si-28.4Cr *in-situ* composite like it has been done previously for NiAl-Cr(Mo) *in-situ* composites.^[30] Geng *et al.*

experimentally verified Nb-10.9Si-28.4Cr to be the ternary eutectic in the Nb-Si-Cr system.^[4] Eutectic *in-situ* composites often exhibit beneficial mechanical properties without adding additional alloying elements. Nanostructuring can be achieved by high quenching rates and temperature gradients as they are present in electron beam remelting (10⁸ to 10⁹ K/m at 10⁴ to 10⁵ m/s^[31]). The cooling rates exceed by far the values in common casting techniques resulting in an extremely fine microstructure. This is due to the small volume of the melt pool. By adjusting the beam parameters like the deflection speed, the energy input and hence solidification conditions (temperature gradient, cooling rate, etc.) can be controlled to realize selective tailoring of the microstructure.^[32] In recent studies, Nb-Si-based alloys have not only been manufactured additively by selective laser beam melting,^[29,33,34] but also by binder jetting and surface electron beam melting.^[24,25] A similar process on a different material system is used in this study. Electron beam melting does not only enable processing of challenging materials like non-weldable nickel-based superalloys,^[35] but also offers the possibility of a crack-free and residual stress-free production by sample preheating. Therefore, electron beam surface remelting is a great tool to check the feasibility of additively processing ternary Nb-Si-Cr *in-situ* composites. The resulting microstructure, mechanical, and oxidation properties are presented in this study.

II. EXPERIMENTAL METHODS

A cigar-shaped Nb-10.9Si-28.4Cr eutectic *in-situ* composite (composition in at. pct) was cast, using arc melting. The 15 × 60 × 6 mm³ size ingot was ground plane parallel and placed onto a standard electron beam melting (EBM) steel baseplate in approximate central position of the build area. The exact position of the specimen with respect to the electron beam was determined by using *in-situ* electron optical imaging and used to calculate the sample coordinates for subsequent remelting.^[36] Remelting was performed under high vacuum conditions at room temperature in an in-house-developed EBM system with an electron beam gun by pro-beam GmbH & Co. KGaA (Gilching, Germany) using a beam current of 7 mA at an acceleration voltage of 60 kV. Four quadratic samples with a side length of 10 mm and a spacing of 2 mm were molten onto the specimen. While the scan velocity was varied from 1000, 500, 250 to 125 mm/s, the scan strategy always was a standard EBM hatch pattern with a line spacing of 100 μm and a rotation of 180 deg between adjacent lines.

For oxidation tests, a slice of each specimen was heat treated in lab air atmosphere for 1 hour at 1200 °C and cooled in air. For microstructural investigations, the sample cross sections were polished using diamond suspension and neutral Oxide Polishing Solution (OPS, 0.025 μm, from Struers GmbH, Willich, Germany). Microstructures were analyzed using a Zeiss Crossbeam 540 FIB/SEM (Focused Ion Beam, Scanning Electron Microscopy) (Zeiss GmbH, Oberkochen, Germany) by

Back-Scattered Electrons (BSE). The overall chemical composition was analyzed via Energy-Dispersive X-ray Spectroscopy (EDS) with an INCA PentaFET-x3 from Oxford Instruments.

X-ray diffraction (XRD) was performed using a Bruker D5000 XRD (Bruker GmbH, Karlsruhe, Germany) operating at 40 kV and a current of 30 mA. A Bragg–Brentano setup was used to record the intensities in a diffraction angle regime of 20 to 120 deg by using $\text{CuK}\alpha$ radiation. The intensities were measured every 0.02 deg for 10 seconds each. The data were analyzed with the DIFFRAC.SUITE EVA commercial software.

Atom Probe Tomography (APT) specimens were prepared by *in-situ* lift-out using a Zeiss Crossbeam 540 FIB/SEM as described in References 37, 38. The APT experiments were carried out in a CAMECA LEAP 4000X HR (CAMECA Inc, Madison, Wisconsin) using pulsed laser mode to trigger field evaporation. An UV laser with 355 nm wavelength at a pulse energy of 75 pJ was used at 200 kHz pulse repetition rate. The specimen base temperature was 55 K. Data processing was done using the commercial software IVAS 3.6.8 from CAMECA Inc., and the implemented reconstruction algorithm published in References 39 and 40. Analyses on the $\text{Nb}_9(\text{Cr},\text{Si})_5$ phase decomposition were done in MATLAB[®] (MathWorks Inc., Natick, MA) with custom programs developed in-house.

The microhardness was determined with a NanoXP Nanoindenter from Keysight (Keysight Technologies Inc., Santa Rosa, CA) using a Berkovich indenter tip geometry. The CSM (continuous stiffness measurement) method was used according to Reference 41 to determine the hardness and stiffness continuously. The maximum indentation depth was 500 nm, and the hardness was averaged over the depth range from 400 to 500 nm.

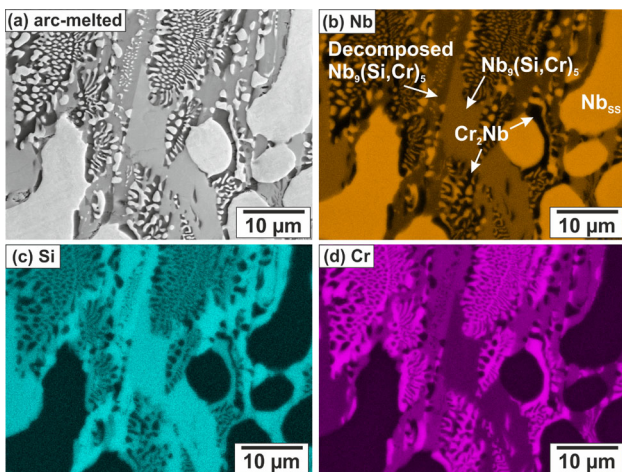


Fig. 1—BSE micrograph of the arc-melted Nb-10.9Si-28.4Cr alloy (a). EDS maps of the region of interest showing the Nb (b), Si (c), and Cr (d) enrichment in the occurring phases Nb_{ss} , Cr_2Nb , and $\text{Nb}_9(\text{Si},\text{Cr})_5$, as well as in the Nb-poor decomposed $\text{Nb}_9(\text{Si},\text{Cr})_5$.

III. RESULTS AND DISCUSSION

A. Arc-Melted Nb-Si-Cr

The arc-melted material in Figure 1 shows a hypoeutectic microstructure consisting of four different phases, Nb_{ss} (white), Cr_2Nb (black), two silicide phases $\text{Nb}_9(\text{Si},\text{Cr})_5$ (light gray), and “decomposed” $\text{Nb}_9(\text{Si},\text{Cr})_5$ (dark gray). The overall composition of the arc-melted material is determined via EDS to be 56.9 ± 1.4 at. pct Nb, 10.7 ± 0.8 at. pct Si, and 32.9 ± 0.8 at. pct Cr, which is slightly off from the eutectic composition of Nb-10.9Si-28.4Cr. The high Nb content in the alloy leads to the formation of Nb dendrites. They are surrounded by a eutectic $\text{Nb}_{\text{ss}}/\text{Cr}_2\text{Nb}/\text{Nb}_9(\text{Si},\text{Cr})_5$ compound, as it is reported in References 10 and 15. All phases were identified with APT according to their chemical composition (see Table I). However, there are apparently two different silicide phases. The $\text{Nb}_9(\text{Si},\text{Cr})_5$ phase, which appears at a lighter gray level in the secondary electron image in Figure 1(a), is rare and

Table I. Phase-Specific Composition of the Arc-Melted Sample, Determined by Atom Probe Tomography

Phase	Nb / at. pct	Si / at. pct	Cr / at. pct
Nb_{ss}	92.7 ± 0.4	0.4 ± 0.2	6.9 ± 0.4
Bright Cr_2Nb	34.4 ± 0.2	13.2 ± 0.4	52.4 ± 0.5
Black $\text{Nb}_9(\text{Cr},\text{Si})_5$	63.9 ± 0.1	16.1 ± 0.4	19.9 ± 0.4
Light Gray Decomposed $\text{Nb}_9(\text{Cr},\text{Si})_5$	54.3 ± 0.2	17.9 ± 0.1	27.7 ± 0.2
Dark Gray			

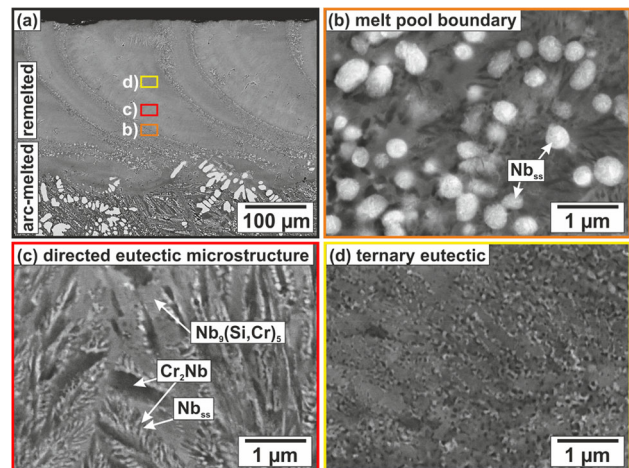


Fig. 2—BSE micrographs of the cross section of the electron beam-remelted layer for the sample processed at a scan velocity of $v = 250$ mm/s (a). Higher magnification images showing coarse spherical Nb_{ss} at the melt pool boundary (b), directed eutectic microstructure of Nb_{ss} and Cr_2Nb near the melt pool boundary (c), and ternary eutectic phase arrangement of Nb_{ss} , Cr_2Nb , and $\text{Nb}_9(\text{Si},\text{Cr})_5$ (d).

mostly occurs in the vicinity of Nb dendrites and consists of 63.9 at. pct Nb. This phase was first reported by Deal *et al.* in 2007 and found to be the matrix phase in many Nb-Si-Cr alloys according to Bewlay *et al.*^[10,27] A darker gray silicide phase in Figure 1(a) is present all over the sample. With a Nb fraction of 54.3 ± 0.2 at. pct and 27.7 ± 0.2 at. pct Cr, it has less Nb and more Cr than the light gray Nb₉(Si,Cr)₅ phase. This indicates that Nb released from the high-temperature Nb₉(Cr,Si)₅ phase diffuses during cooling to the surrounding Nb_{ss} phases. Apparently, the dark gray Nb₉(Cr,Si)₅ phase represents a Nb-poor Nb₉(Cr,Si)₅ phase that decomposed simultaneously in Cr₂Nb and Nb₅Si₃ and is labeled as “decomposed” Nb₉(Si,Cr)₅. However, this is not visible in SEM and explained in Figure 4 in more detail.

B. Nanostructured Nb-Si-Cr

On the surface of the arc-melted specimen, the surface layer was remelted using an electron beam. The result is a very fine microstructure with phases in the regime of 10 to 100 nm (see Figure 2). The scan velocity, the only parameter that was varied in the process, strongly affects the energy input, the melt pool size, and therefore, the solidification conditions. A small melt pool depth results from fast scan rates. Hence, cooling of the melt is rapid. The layer thickness is 480 ± 20 μm for the slowest scan velocity ($v = 125$ mm/s) and goes down to 74 ± 5 μm for the fastest scan velocity ($v = 1000$ m/s). All samples consist of equivalent microstructures in-between u-shaped boundaries of the melt pool. These boundaries can be found in a distance of 100 μm from each other, indicating the pre-set line offset of the scan strategy. There are coarse spherical Nb_{ss} precipitates due to high nucleation rate at the bottom of the melt pool and subsequent heat treatment by heat flux from the melt [Figure 2(b)]. Figure 2(c) shows directional eutectic growth near the melt pool boundary. Especially, Cr₂Nb is growing along the temperature gradient towards the surface of the sample. With increasing distance from the melt pool boundary in Figure 2(d), the eutectic microstructure loses its preferred growth direction and uniformly distributed phases form in a non-oriented eutectic arrangement.

Figure 2 does not show cracks present in the electron beam-remelted layer. However, high-temperature gradients during remelting and subsequent thermal shock induce networks of cracks in the layer. In a real powder bed-based process, the sample will be preheated, and layers will be remolten partially to reduce thermal stresses and minimize crack formation. The overall chemical composition of the remelted layer is 59.0 ± 0.7 at. pct Nb, 11.5 ± 0.7 at. pct Si, and 29.5 ± 1.3 at. pct Cr. It is similar for all samples and does not vary with different scan velocities. Parts of the Cr are evaporating during electron beam remelting due to its high vapor pressure in a vacuum atmosphere,^[42] so the remelted layer exhibits a composition very close to the ternary eutectic. Also, the high freezing rate enables the creation of a eutectic microstructure, even for hypoeutectic alloys

due to forced supersaturation of the phases (see Table II).

C. Phase-Specific Analysis

The alloy is very close to the eutectic composition and according to the liquidus surface projection, the eutectic solidification proceeds immediately from the melt: $L \rightarrow \text{Nb}_9(\text{Cr, Si})_5 + \text{Nb}_{\text{ss}} + \text{Cr}_2\text{Nb}$ with high amounts of Nb₉(Cr, Si)₅. The rapid cooling suppresses diffusion and phase growth, so nanostructured phases form aligned along the temperature gradient. Figure 3 displays the phase refinement with the increase in freezing rates generated by the increase in scan velocities. For fast scan rates ($v = 1000$ mm/s), only a small melt pool is generated and the sudden solidification by self-quenching is very fast. In addition, the solid-liquid interface is instable and non-planar, leading to small and irregular colonies of eutectic phase growth with non-aligned phases that are 10 times smaller than in the arc-melted material. Previous studies have already confirmed electron beam remelting to be a suitable process for creating nanostructured *in-situ* composites, where immiscible eutectic systems are able to form phases smaller than 10 nm.^[30] In the case of Nb-Si-Cr, the phases are also in the regime of 10 nm, but their irregular shape prohibits an accurate measurement of phase diameter. For slower scan rates ($v = 250$ mm/s and $v = 125$ mm/s), especially the Cr₂Nb and Nb_{ss} phases are coarser. The silicide phase Nb₉(Cr,Si)₅ is the matrix phase with the highest volume fraction in all specimen. Nb_{ss} and Cr₂Nb are present in each sample and their chemical composition given in Table II is in reasonable agreement with Reference 4. Furthermore, small and spherical Nb₅Si₃ phases are found in the specimen processed with fast scan velocities. Despite high solidification rates, the metastable phase Nb₃Si was not found as reported in other studies.^[19] For slow scan rates (250 mm/s and 125 mm/s), the decomposed Nb₉(Cr,Si)₅ phase becomes pronounced, like in the arc-melted material.

The chemical composition of the observed phases in all samples according to Table 2 can be plotted in a Nb-Si-Cr ternary phase diagram. Figure 4 shows the Nb-rich corner of an isothermal section of this system. For slower solidification, the phases exhibit a composition closer to equilibrium, displayed by the arc-melted sample. The stoichiometric compositions, however, are not reached entirely. Non-equilibrium solidification conditions due to fast quenching rates suppress diffusion and force solidification of supersaturated phases. The Nb content is reduced in Nb_{ss} and Nb₅Si₃, but is enriched in Cr₂Nb and Nb₉(Cr,Si)₅ with the increase in cooling rate. The Cr content rises in Nb_{ss} and Nb₅Si₃ for high scan rates. Si only enriches in Cr₂Nb for the fast solidified condition. The atom probe revealed a significant amount of 12.5 at. pct Si substituting for Cr in Cr₂Nb. This leads to the stabilization of C14 Cr₂Nb (*P63/mmc*) down to room temperature. For reasons of simplicity, the C14 Cr₂Nb phase is shortened to Cr₂Nb hereafter. The formation of Nb_{ss} and Cr₂Nb is preferred since both phases are able to solute high amounts of foreign atoms. Their stoichiometry is not limited to a

Table II. Composition of All Phases in the Specimen Processed at Scan Speeds of 1000, 500, 250, and 125 mm/s, Determined by Atom Probe Tomography

Scan Speed (mm/s)	Phase	Nb (At. Pct)	Si (At. Pct)	Cr (At. Pct)
125	Nb _{ss}	88.4 ± 0.6	1.0 ± 0.2	10.4 ± 0.5
	Cr ₂ Nb	36.3 ± 1.5	12.4 ± 0.4	51.3 ± 1.6
	Nb ₅ Si ₃	—	—	—
	Nb ₉ (Cr,Si) ₅	64.2 ± 0.3	15.8 ± 0.6	19.9 ± 0.5
	Decomposed Nb ₉ (Cr,Si) ₅	54.0 ± 1.1	17.9 ± 0.9	28.1 ± 1.9
250	Nb _{ss}	86.7 ± 1.5	1.2 ± 0.4	11.8 ± 1.0
	Cr ₂ Nb	40.2 ± 1.8	9.6 ± 1.2	50.1 ± 1.7
	Nb ₅ Si ₃	—	—	—
	Nb ₉ (Cr,Si) ₅	65.9 ± 1.2	12.5 ± 1.2	21.4 ± 0.9
	Decomposed Nb ₉ (Cr,Si) ₅	55.7 ± 0.6	17.7 ± 1.1	26.4 ± 0.5
500	Nb _{ss}	86.2 ± 0.5	2.1 ± 0.1	11.6 ± 0.5
	Cr ₂ Nb	44.4 ± 0.7	12.9 ± 1.7	42.6 ± 2.0
	Nb ₅ Si ₃	66.1 ± 3.7	30.3 ± 4.9	3.2 ± 1.3
	Nb ₉ (Cr,Si) ₅	64.2 ± 3.3	11.3 ± 0.4	24.3 ± 3.6
	Decomposed Nb ₉ (Cr,Si) ₅	—	—	—
1000	Nb _{ss}	83.3 ± 0.5	3.2 ± 0.5	13.5 ± 0.9
	Cr ₂ Nb	46.3 ± 1.7	12.5 ± 3.1	41.1 ± 2.4
	Nb ₅ Si ₃	65.5 ± 2.5	30.0 ± 3.6	4.4 ± 1.2
	Nb ₉ (Cr,Si) ₅	68.9 ± 1.9	10.4 ± 0.5	20.7 ± 1.6
	Decomposed Nb ₉ (Cr,Si) ₅	—	—	—

Three different phases of each kind were analyzed to determine the standard deviation of their composition.

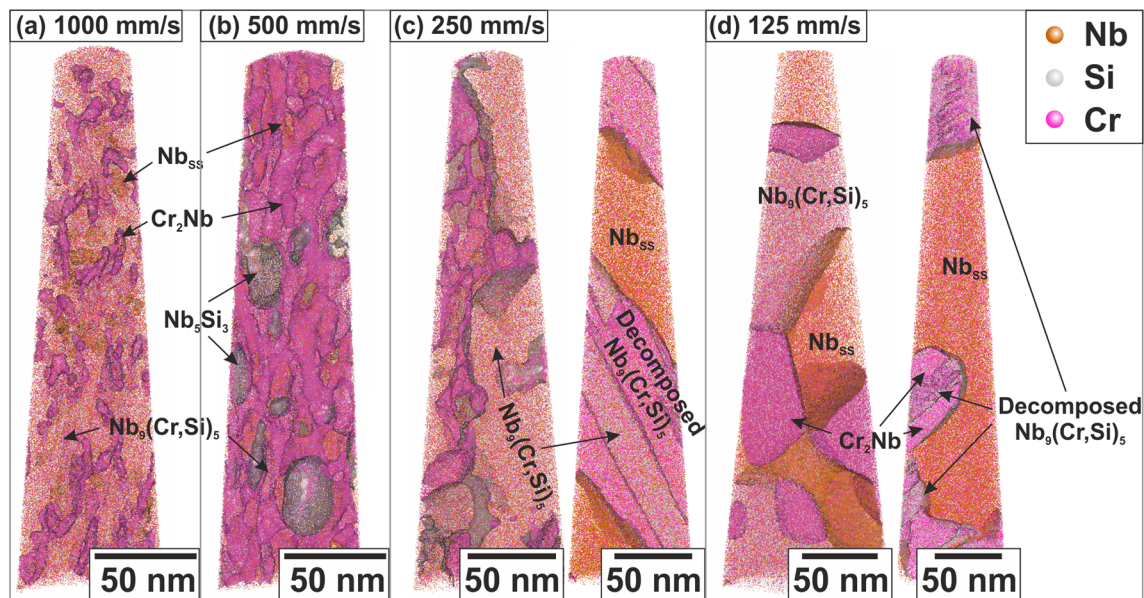


Fig. 3—Atom probe tomographies of the electron beam-remelted samples manufactured with a scan velocity of $v = 1000$ mm/s (a), 500 mm/s (b), 250 mm/s (c), and 125 mm/s (d) (Color figure online).

very narrow region in the phase diagram. Also, the mixed silicide phase Nb₉(Cr,Si)₅ is favored at fast freezing rates due to its variable stoichiometry. The displayed phase diagram only considers diagrammatic data from Shao *et al.*^[13] and the incorporation of Cr into the binary silicides is not taken into account. Despite the narrow single-phase region of α -Nb₅Si₃ in Figure 4, a

significant amount of 4.4 at. pct Cr is solved in Nb₅Si₃. This Cr incorporation into binary silicides has already been proposed and calculated by David *et al.* and Steinmetz *et al.*^[43–46] The solubility of Cr in the Nb₅Si₃ phase and other silicide phases therefore have to be taken into account and a new phase diagram has to be calculated in future research also including the existence

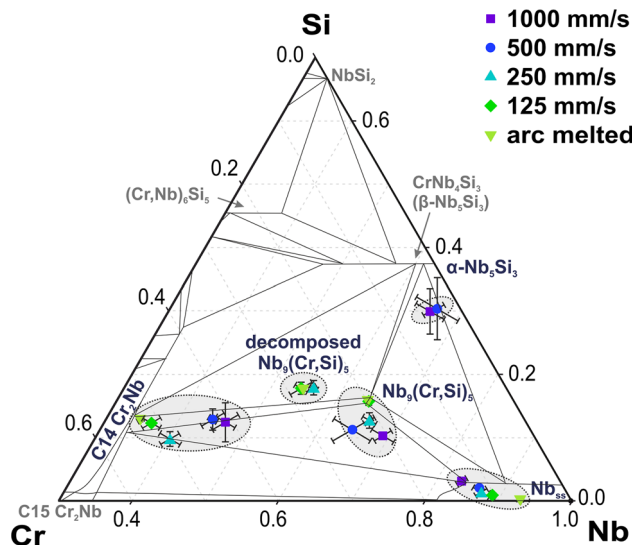


Fig. 4—Isothermal section of the Nb-rich corner in the Nb-Si-Cr phase diagram at 1400°C according to Varma *et al.*^[47] Every dot represents the average chemical composition of a phase determined by atom probe tomography in arc-melted and nanostructured Nb-Si-Cr composite. In this phase diagram, the composition of the decomposed $Nb_9(Cr,Si)_5$ is plotted as average composition of the parallel Nb_5Si_3 and Cr_2Nb plates.

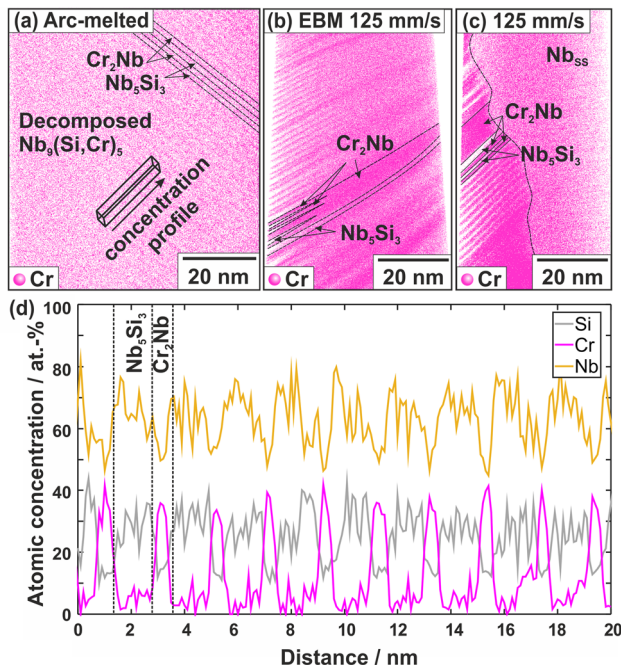


Fig. 5—Atom probe tomographies showing the phase decomposition in the Nb-poor $Nb_9(Cr,Si)_5$ phase in arc-melted material (a) and remelted layer (b, c) with a scan speed of 125 mm/s. A region of interest cropped out of the tomography in (a) and a 1D concentration profile perpendicular to the Cr-rich layers was calculated, showing the lamellar decomposition of Nb-poor $Nb_9(Cr,Si)_5$ (d).

of $Nb_9(Si, Cr)_5$. However, for reasons of simplicity this phase diagram has not been modified and is identical to that proposed by Varma *et al.*^[47]

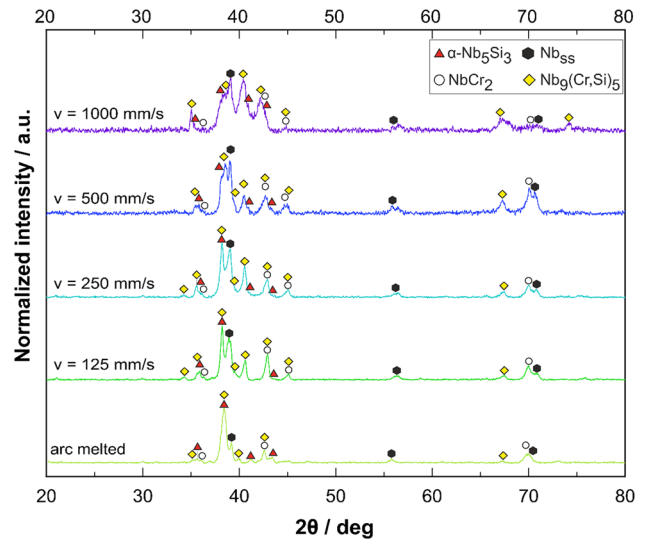


Fig. 6—X-ray diffraction pattern of the arc-melted specimen and all electron beam-melted layers, processed with a scan velocity of $v = 125$ mm/s, $v = 250$ mm/s, $v = 500$ mm/s, and $v = 1000$ mm/s.

D. Decomposition of $Nb_9(Cr,Si)_5$

The decomposed $Nb_9(Cr,Si)_5$ phase can be identified in the arc-melted material as well as in the EBM samples processed with slow scan speeds of 125 and 250 mm/s. The $Nb_9(Cr,Si)_5$ phase decomposes under the formation of small spherical Nb_{ss} precipitates or with Nb diffusion towards a neighboring Nb_{ss} phase [Figure 5(c)]. The Nb content in the $Nb_9(Cr,Si)_5$ phase decreases from 65 at. pct to 54 at. pct. This silicide phase with 54 at. pct Nb was detected in previous investigations, but was neither studied nor identified. Bewlay *et al.* labeled this phase as $Nb_9(Cr,Si)_5 + Nb_{ss}$.^[4,10] However, within the loss in Nb, the silicide phase simultaneously decomposes in the stable phases $\alpha-Nb_5Si_3$ and Cr_2Nb (see Figure 5). Precise atom probe analysis of this phase transition shows a solid-state phase transformation in a Cr-rich and a Cr-poor phase on an atomic scale. Figure 5(d) shows a 1D (one-dimensional) concentration profile perpendicular to the Cr-rich plates. Since the Cr-poor phase barely shows any Cr and more than 60 at. pct Nb and 30 at. pct Si, it can be identified to be $\alpha-Nb_5Si_3$. The Cr-rich phase is Cr_2Nb , respectively. There is twice as much Nb_5Si_3 formed than Cr_2Nb . Their exact chemical composition could not be determined for thin atomic layers with APT experiments due to local magnification, hence the 1D concentration profile is the only way for phase identification.^[48] The two phases are in parallel lamellar arrangement with a constant distance of 2 nm. This is possible, since both $\alpha-Nb_5Si_3$ and the parent $Nb_9(Cr,Si)_5$ have tetragonal $I4/mcm$ (140) space group. In contrast to the remelted layers in Figures 4(b) and (c), the two phases in the arc-melted material are equally spaced due to uniform solidification. Since electron beam surface remelting leads to extremely different local solidification conditions, the freezing rate is slower at some points and thicker lamellae can be formed. This is in agreement with the XRD measurements, since no

other silicide phases were found, and all peaks can be related to the mentioned phases (see Figure 6).

The $\text{Nb}_9(\text{Cr,Si})_5$ in the arc-melted sample is very rare and prefers the vicinity of primarily solidified Nb dendrites. For the arc-melted sample, that was heat treated for 1 hour at 1200 °C, no $\text{Nb}_9(\text{Cr,Si})_5$ was found and the whole silicide matrix shows a Nb content of 54 at. pct. Supersaturation forced by non-equilibrium solidification in electron beam remelting is the reason for the occurrence of the high-temperature phase $\text{Nb}_9(\text{Cr,Si})_5$ at room temperature. This phase is known to decompose after a heat treatment at 1300 °C with the formation of $\alpha\text{-Nb}_5\text{Si}_3$, Cr_2Nb , and Nb_{ss} .^[4]

E. X-ray Diffraction

X-ray diffraction was used to identify the phases A2 $Im\bar{3}m$ Nb_{ss} , C14 $P63/mmc$ Cr_2Nb , D8₁ $I4/mcm$ $\alpha\text{-Nb}_5\text{Si}_3$, and $I4/mcm$ $\text{Nb}_9(\text{Cr,Si})_5$ due to their crystal structure-specific diffraction pattern (Figure 6). The $\text{Nb}_9(\text{Cr,Si})_5$ phase was determined by using the crystal structure and the lattice parameters of the $I4/mcm$ Nb_9SiCr_4 phase from Reference 27 and by simulating a crystal diffraction pattern similar to that described in References 10 and 27. In addition, SEM EBSD was used in both the arc-melted and the remelted specimen to support phase identification. The pattern matched the pattern observed in References 4 and 27. In the arc-melted material, there is a strong peak at 39 deg. This peak is present in all samples. It results from both the $\alpha\text{-Nb}_5\text{Si}_3$ phase and $\text{Nb}_9(\text{Cr,Si})_5$ phase. However, the other peaks for $\text{Nb}_9(\text{Cr,Si})_5$ are less pronounced in the arc-melted material, so a higher amount of $\alpha\text{-Nb}_5\text{Si}_3$ is expected. In the electron beam-remelted layers with their nanocrystalline microstructures, the relative intensities of the $\text{Nb}_9(\text{Cr,Si})_5$ peaks become very pronounced and $\alpha\text{-Nb}_5\text{Si}_3$ peaks decrease with the rise in solidification velocity. Especially for the layers melted with $v = 500$ mm/s and $v = 1000$ mm/s, the peaks of $\text{Nb}_9(\text{Cr,Si})_5$ and Nb_{ss} exceed the $\alpha\text{-Nb}_5\text{Si}_3$ peak. In addition to the atom probe experiments, also the X-ray diffraction pattern (Figure 6) indicates a shift of the microstructure from $\alpha\text{-Nb}_5\text{Si}_3$ towards a higher amount of $\text{Nb}_9(\text{Cr,Si})_5$ phases with the increase in solidification

rates. The diffraction pattern of the sample processed at $v = 1000$ mm/s exhibits very broad peaks with a significant lower maximum intensity compared to the arc-melted specimen. The diffraction pattern do not show any crystal structures of other silicide phases than the mentioned $\alpha\text{-Nb}_5\text{Si}_3$ and $\text{Nb}_9(\text{Cr,Si})_5$. This is in very good agreement with the atom probe experiments. Due to the nanostructured phases present in the electron beam-melted layers, the background is higher and the peaks are broader. This can be attributed to the presence of small crystallite sizes, high microstresses, high dislocation densities, coherency strains, and chemical inhomogeneities as it is the case in the electron beam-melted layers.^[49] In other studies, the $\text{Nb}_9\text{Cr}_2\text{Si}_3$ is mentioned to be stable at room temperature.^[11] This is not the case for an Nb-10.9Si-28.4Cr *in-situ* composite, where XRD and APT measurements both verify a decreasing amount of $\text{Nb}_9(\text{Cr,Si})_5$ for slow freezing rates. The phase diagram has to be modified, since no $\text{Nb}_9\text{Cr}_x\text{Si}_y$ ($x + y = 5$) phases are apparently stable at room temperature.

F. Hardness

In Figure 7, the hardness of ternary eutectics in the arc-melted part and the EBM layer are compared. In the latter, the exceptional fine microstructure leads to a high hardness of more than 15 GPa, which is significantly higher than 10.9 ± 2.1 GPa of the ternary eutectic in the arc-melted part. The hardness of the Nb_{ss} in the arc-melted material is 7.4 ± 0.5 GPa which is higher than that of pure Nb due to solid solution strengthening. The silicide phase in the arc-melted material has a hardness of 14.8 ± 1.0 GPa due to the hard and brittle character of silicides and the phase decomposition yielding to a small-scale lamellar composite. The Laves phase Cr_2Nb in the arc-melted material is in the regime of 10.8 ± 1.3 GPa. In the nanostructured layer, the phase refinement by rapid solidification is the main reason for the higher hardness. Plenty phases are tested with one single nanoindent, so hardening can be attributed to Hall–Petch-like strengthening.^[50] A minor amount can also be attributed to solid solution strengthening, since atom probe experiments have shown up to 15 at. pct foreign atoms in Cr_2Nb and Nb_{ss} . Residual stresses and textured phases present in the remelted layer only affect the hardness to a minor degree.^[51] In the case of nanoindentation, textured phases lead to anisotropic pile-ups, but this does not influence hardness values to a major extent.^[52]

G. Oxidation

Oxidation tests at 1200 °C for 1 hour reveal a layered structure in the oxide scale of the arc-melted sample. For the arc-melted material, the oxide layer is often spalled or cracked and not adherent to the metal surface. Figure 8 clearly shows cracks at the interface of the oxide layer and the *in-situ* composite. These surface cracks are crucial to oxidation by causing local penetration of oxygen leading to irregular and excessive growth of the oxide layer. In unfavorably oriented

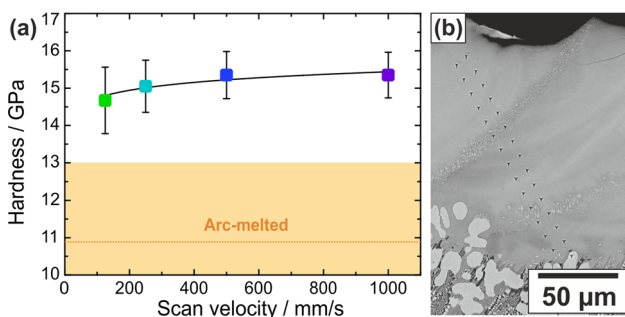


Fig. 7—Hardness of ternary eutectics in the electron beam-remelted layers (dots with error bars) as a function of the scan velocity and in the arc-melted area for comparison (dashed line with colored standard deviation) (a) determined by nanoindentation across the cross section of the surface layer (b) (Color figure online).

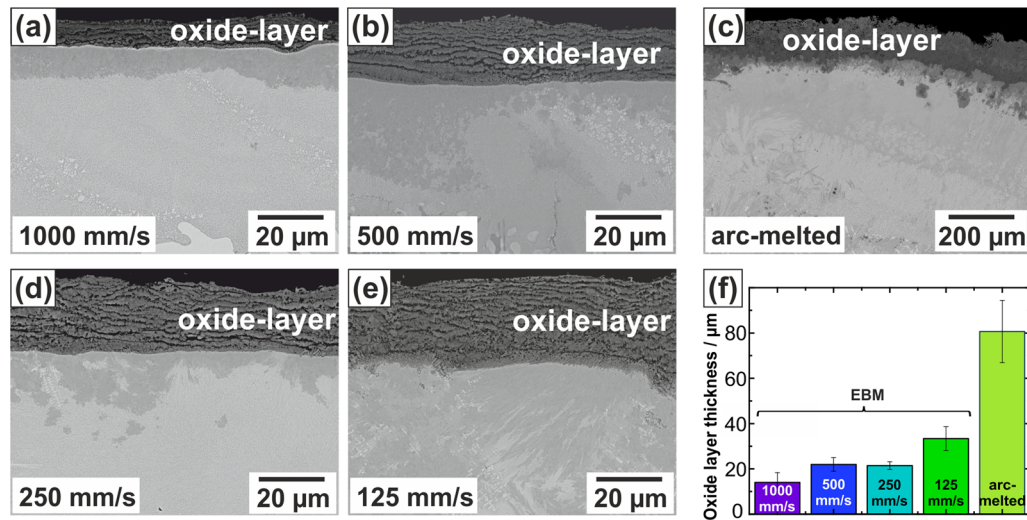


Fig. 8—BSE cross sections of the sample processed with a scan speed of $v = 1000$ mm/s to $v = 125$ mm/s (a, b, d, e) and the arc-melted sample (c) that were heat treated at 1200 °C for 1 h in air atmosphere, forming a surface oxide layer. The resulting oxide layer thickness for each tested specimen is plotted in (f).

interphases and near phases with low oxidation resistance like Nb dendrites, the oxide growth is accelerated. However, the oxide layer of the nanostructured material processed by electron beam melting exhibits uniform thickness and significantly less cracking is observed. The surface is rather smooth and a smaller layer thickness of the Cr and Nb oxides is present. Due to the small crystallite size, the influence of texture on the oxidation behavior is less significant than it is for interfaces in the arc-melted material. However, spherical Nb precipitates at the melt pool boundary are still preferred sites for fast oxidation. All occurring oxides have been identified by means of SEM-EDS and EBSD and are similar to those reported for Nb-Si-Cr-based alloys in other studies.^[53] The alternating layers of oxides are Nb_5O_2 and CrNbO_4 with small amounts of Cr_2O_3 and SiO_2 , which is in agreement with X-ray diffraction measurements on similar alloys from References 11, 20, 53, and 54. The BSE micrographs in this study do not show an outer and inner oxide layer as it is reported by Reference 29. Underneath the oxide layer, a gray oxygen-rich area can be found with a thickness of 10 to $50 \mu\text{m}$. These zones consist of the Nb_{ss} phase with a high oxygen content in solid solution, which was confirmed by EDS mappings and appear with dark gray color in BSE imaging. At high temperatures of 1200 °C, the diffusion of oxygen in Nb is enhanced due to its high solubility in Nb.^[29,55] In the arc-melted specimen, these gray areas can be found especially in and around Nb dendrites. In the EBM layer, the finely dispersed and separated Nb particles hinder oxygen diffusion through the Nb phase over a long distance and the gray layer is smaller. It also depends on the texture of the microstructure, so in elongated phases and near the boundary of the melt pool, the gray oxygen-rich zones are larger. Also surface cracking will affect the appearance of these zones.

The electron beam-melted layer possesses a four times smaller oxide layer thickness than found on the arc-melted sample [Figure 8(f)]. First and foremost,

the reason for enhanced oxidation resistance is the refinement of phases with weak oxidation behavior like Nb_{ss} , leading to a higher interface area for Nb_{ss} but especially for silicide phases. Hence, the oxygen partial pressure is averaged on many silicide interfaces, and Nb_{ss} interphases suffer from a much lower oxygen partial pressure. Furthermore, finely dispersed silicides can create a glassy SiO_2 layer that can protect other phases from oxidation.^[56] The high amount of Si and Cr supersaturated in the Nb_{ss} phase also increases its oxidation resistance. The formation of non-protective internal oxide Nb_2O_5 is suppressed by the growth of CrNbO_4 mixed oxide. The improvement in oxidation resistance by phase refinement is consistent with the previous results found by Guo *et al.* for fine-structured samples of a Nb-Si-Ti-Cr-Al-Hf alloy processed by selective laser beam melting.^[29] In the present study, another positive effect on oxidation behavior was observed. Fast solidification can lead to metastable $\text{Nb}_9(\text{Cr},\text{Si})_5$ at room temperature. This leads to less Nb_{ss} present in the alloy. Furthermore, during high-temperature oxidation, this phase will of course decompose. This results in further phase refinement of the microstructure during heat treatment and the positive effect of fine phases on oxidation is enhanced.

IV. SUMMARY AND CONCLUSION

This paper highlights a nanostructured microstructure of a eutectic Nb-Si-Cr *in-situ* composite, generated by electron beam remelting. Microstructure, phase formation, and their effect on oxidation behavior were studied, and the following conclusions can be drawn:

1. High quenching rates lead to a nanostructured material with phase diameters less than 10 nm, leading to an increased hardness up to 15.3 GPa.

2. Non-equilibrium solidification favors the formation of C14 Cr₂Nb and metastable Nb₉(Cr,Si)₅ due to their variable stoichiometry. The phase fraction of the silicide phase increases with cooling rate.
3. The metastable Nb₉(Cr,Si)₅ decomposes into α-Nb₅Si₃ and Cr₂Nb in a lamellar arrangement after diffusional loss of Nb_{ss}. Nb₉(Cr,Si)₅ and α-Nb₅Si₃ are the only silicide phases present in eutectic and near-eutectic Nb-Si-Cr alloys.
4. Nanostructured phases as well as metastable mixed silicides like Nb₉(Cr,Si)₅ are able to increase the oxidation resistance for Nb-SiCr *in-situ* composites up to four times compared to the arc-melted material.

Therefore, selective electron beam melting is a quiet attractive process not only for manufacturing of bulk samples of Nb-Si-Cr, but also as a surface treatment to improve the mechanical and the oxidation behavior of Nb-Si-Cr alloys.

ACKNOWLEDGMENTS

The authors acknowledge funding of the atom probe by the Deutsche Forschungsgemeinschaft (DFG) via the Cluster of Excellence ‘Engineering of Advanced Materials’ (Project EXC 315). The authors also would like to acknowledge the chair for materials science and engineering for metals at FAU Erlangen-Nürnberg for sample processing, collaboration, and advice.

AUTHOR CONTRIBUTIONS

AF wrote the main manuscript text and performed, analyzed and interpreted SEM imaging, EDS measurements as well as atom probe experiments. JV performed and analyzed sample preparation, heat treatments, and Nanoindentation experiments. DH performed and interpreted XRD measurements. CA fabricated samples via EBM and wrote the additive manufacturing section of the paper. SN revised the main text, interpreted data, and designed the study. PF programmed a MatLab code to analyze the phase decomposition in the APT data. MG drafted and substantively revised this work. All authors reviewed the manuscript.

FUNDING

Open Access funding enabled and organized by Projekt DEAL.

CONFLICT OF INTEREST

The authors declare that they have no conflict of interests.

OPEN ACCESS

This article is licensed under a Creative Commons Attribution 4.0 International License, which permits

use, sharing, adaptation, distribution and reproduction in any medium or format, as long as you give appropriate credit to the original author(s) and the source, provide a link to the Creative Commons licence, and indicate if changes were made. The images or other third party material in this article are included in the article’s Creative Commons licence, unless indicated otherwise in a credit line to the material. If material is not included in the article’s Creative Commons licence and your intended use is not permitted by statutory regulation or exceeds the permitted use, you will need to obtain permission directly from the copyright holder. To view a copy of this licence, visit <http://creativecommons.org/licenses/by/4.0/>.

REFERENCES

1. B.P. Bewlay, M.R. Jackson, J.-C. Zhao, P.R. Subramanian, M.G. Mendiratta, and J.J. Lewandowski: *MRS Bull.*, 2003, vol. 28, pp. 646–53.
2. N. Wang, L. Jia, B. Kong, Y. Guo, H. Zhang, and H. Zhang: *Int. J. Refract Metal Hard Mater.*, 2018, vol. 71, pp. 273–79.
3. M.E. Schlesinger, H. Okamoto, A.B. Gokhale, and R. Abbaschian: *J. Phase Equilib.*, 1993, vol. 14, pp. 502–09.
4. F. Gang, A. Kauffmann, and M. Heilmaier: *Metall. Mater. Trans. A*, 2018, vol. 49A, pp. 763–71.
5. B.P. Bewlay, M.R. Jackson, and P.R. Subramanian: *JOM*, 1999, vol. 51, pp. 32–36.
6. J.-C. Zhao and J.H. Westbrook: *MRS Bull.*, 2003, vol. 28, pp. 622–30.
7. D.L. Davidson: *Metall. Mater. Trans. A.*, 1997, vol. 28A, pp. 1297–1314.
8. D.L. Davidson, K.S. Chan, and D.L. Anton: *Metall. Mater. Trans. A.*, 1996, vol. 27A, pp. 3007–18.
9. J.D. Rigney, P.M. Singh, and J.J. Lewandowski: 1992, p. 6.
10. B.P. Bewlay, Y. Yang, R.L. Casey, M.R. Jackson, and Y.A. Chang: *Intermetallics*, 2009, vol. 17, pp. 120–27.
11. B. Voglewede, V.R. Rangel, and S.K. Varma: *Corros. Sci.*, 2012, vol. 61, pp. 123–33.
12. K.S. Chan: *Mater. Sci. Eng. A*, 2002, vols. 329–331, pp. 513–22.
13. G. Shao: *Intermetallics*, 2005, vol. 13, pp. 69–78.
14. J. Geng, P. Tsakiroopoulos, and G. Shao: *Intermetallics*, 2006, vol. 14, pp. 227–35.
15. J. Geng, G. Shao, and P. Tsakiroopoulos: *Intermetallics*, 2006, vol. 14, pp. 832–37.
16. P. Tsakiroopoulos: *Materials*, 2018, vol. 11, p. 592.
17. H.J. Goldschmidt and J.A. Brand: *J. Less Common Met.*, 1961, vol. 3, pp. 34–43.
18. J.-C. Zhao, M. Jackson, and L. Peluso: *Acta Mater.*, 2003, vol. 51, pp. 6395–6405.
19. L. Su, L. Jia, Y. Feng, H. Zhang, S. Yuan, and H. Zhang: *Mater. Sci. Eng. A*, 2013, vol. 560, pp. 672–77.
20. K.S. Chan: *Oxid. Met.*, 2004, vol. 61, pp. 165–94.
21. S.K. Varma, C. Parga, K. Amato, and J. Hernandez: *J. Mater. Sci.*, 2010, vol. 45, pp. 3931–3937.
22. B.P. Bewlay, M.R. Jackson, and H.A. Lipsitt: *Metall. Mater. Trans. A.*, 1996, vol. 27A, pp. 3801–08.
23. P. Subramanian, M. Mendiratta, D. Dimiduk, and M. Stucke: *Mater. Sci. Eng., A*, 1997, vols. 239–240, pp. 1–13.
24. Y. Guo, J. He, Z. Li, L. Jia, H. Su, J. Zhang, and H. Zhang: *Corros. Sci.*, 2020, vol. 163, p. 108281.
25. Y. Guo, Z. Li, J. He, H. Su, L. Jia, J. Zhang, L. Liu, and H. Zhang: *Mater. Charact.*, 2020, vol. 159, p. 110051.
26. B.P. Bewlay, J.J. Lewandowski, and M.R. Jackson: *JOM*, 1997, vol. 49, pp. 44–45.
27. A. Deal, W. Heward, D. Ellis, J. Cournoyer, K. Dovidenko, and B. Bewlay: *Microsc. Microanal.*, 2007, vol. 13, pp. 90–91.
28. N. Sekido, Y. Kimura, S. Miura, F.-G. Wei, and Y. Mishima: *J. Alloy Compd.*, 2006, vol. 425, pp. 223–29.

29. Y. Guo, L. Jia, B. Kong, F. Zhang, J. Liu, and H. Zhang: *Corros. Sci.*, 2017, vol. 127, pp. 260–69.
30. A. Förner, S. Giese, C. Arnold, P. Felfer, C. Körner, S. Neumeier, and M. Göken: *Sci. Rep.*, 2020, vol. 10, pp. 1–9.
31. C. Körner: *Int. Mater. Rev.*, 2016, vol. 61, pp. 361–77.
32. N. Raghavan, S. Simunovic, R. Dehoff, A. Plotkowski, J. Turner, M. Kirka, and S. Babu: *Acta Mater.*, 2017, vol. 140, pp. 375–87.
33. Y. Guo, L. Jia, S. Sun, B. Kong, J. Liu, and H. Zhang: *Mater. Des.*, 2016, vol. 109, pp. 37–46.
34. Y.-L. Guo, L.-N. Jia, B. Kong, Y.-L. Huang, and H. Zhang: *Acta Metall. Sin. (Eng. Lett.)*, 2018, vol. 31, pp. 477–86.
35. M. Ramsperger, R.F. Singer, and C. Körner: *Metall. Mater. Trans. A.*, 2016, vol. 47A, pp. 1469–80.
36. C. Arnold, C. Pobel, F. Osmanlic, and C. Körner: *Rapid Prototyp. J.*, 2018, vol. 24, pp. 1401–06.
37. K. Thompson, D. Lawrence, D.J. Larson, J.D. Olson, T.F. Kelly, and B. Gorman: *Ultramicroscopy*, 2007, vol. 107, pp. 131–39.
38. M.K. Miller, K.F. Russell, K. Thompson, R. Alvis, and D.J. Larson: *Microsc. Microanal.*, 2007, vol. 13, pp. 428–36.
39. P. Bas, A. Bostel, B. Deconihout, and D. Blavette: *Appl. Surf. Sci.*, 1995, vols. 87–88, pp. 298–304.
40. B. Gault, D. Haley, F. de Geuser, M.P. Moody, E.A. Marquis, D.J. Larson, and B.P. Geiser: *Ultramicroscopy*, 2011, vol. 111, pp. 448–57.
41. W.C. Oliver and G.M. Pharr: *J. Mater. Res.*, 1992, vol. 7, pp. 1564–83.
42. E.A. Gulbransen and K.F. Andrew: *J. Electrochem. Soc.*, 1952, vol. 99, p. 402.
43. N. David, Y. Cartigny, T. Belmonte, J.M. Fiorani, and M. Vilasi: *Intermetallics*, 2006, vol. 14, pp. 464–73.
44. J. Steinmetz, B. Malaman, and B. Roques: *J. Less-Common Met.*, 1978, vol. 57, pp. 133–46.
45. M. Vilasi, M. Francois, R. Podor, and J. Steinmetz: *J. Alloy Compd.*, 1998, vol. 264, pp. 244–51.
46. M. Vilasi, P. Steinmetz, and J. Steinmetz: *J. Less Common Met.*, 1991, vol. 175, pp. L7–10.
47. S.K. Varma, C. Parga, K. Amato, and J. Hernandez: *J. Mater. Sci.*, 2010, vol. 45, pp. 3931–37.
48. M.K. Miller and M.G. Hetherington: *Surf. Sci.*, 1991, vol. 246, pp. 442–49.
49. T. Ungár: *Scripta Mater.*, 2004, vol. 51, pp. 777–81.
50. E.O. Hall: *Proc. Phys. Soc. Sect. B*, 1951, vol. 64, pp. 747–53.
51. T.Y. Tsui, W.C. Oliver, and G.M. Pharr: *J. Mater. Res.*, 1996, vol. 11, pp. 752–59.
52. M. Göken, M. Kempf, and W.D. Nix: *Acta Mater.*, 2001, vol. 49, pp. 903–11.
53. W. Jiang, W. Shao, J. Sha, and C. Zhou: *Prog. Nat. Sci. Mater. Int.*, 2018, vol. 28, pp. 740–48.
54. K.S. Chan: *Metall. Mater. Trans. A*, 2004, vol. 35, pp. 589–97.
55. J. Zheng, X. Hou, X. Wang, Y. Meng, X. Zheng, and L. Zheng: *Corros. Sci.*, 2015, vol. 96, pp. 186–95.
56. W. Wei, H. Wang, C. Zou, Z. Zhu, and Z. Wei: *Mater. Des.*, 2013, vol. 46, pp. 1–7.

Publisher's Note Springer Nature remains neutral with regard to jurisdictional claims in published maps and institutional affiliations.